Two-dimensional thermoelectrics with Rashba spin-split bands in bulk BiTeI

Lihua Wu,[1,2,3] Jiong Yang,[1] Shanyu Wang,[1] Ping Wei,[1] Jihui Yang,[1,*] Wenqing Zhang,[2,4,†] and Lidong Chen[2]

[1]*Materials Science and Engineering Department, University of Washington, Seattle 98195, Washington, USA*

[2]*State Key Laboratory of High Performance Ceramics and Superfine Microstructure, Shanghai Institute of Ceramics, Chinese Academy of Sciences, Shanghai 200050, China*

[3]*University of Chinese Academy of Sciences, Beijing 100049, China*

[4]*Materials Genome Institute, Shanghai University, Shanghai 200444, China*

(Received 22 May 2014; revised manuscript received 27 October 2014; published 26 November 2014)

The Rashba effect is interesting for thermoelectrics because of the unique spin-splitting band structure. By using bulk BiTeI with a giant Rashba effect as an example, we prove that the spin-splitting-induced constant density of states leads to a two-dimensional thermopower. The thermopower is higher as compared with that in spin-degenerate bands, primarily due to the lower Fermi level in the Rashba spin-splitting bands at given carrier concentrations. A quantitative relation between thermopower and the Rashba parameter is established. Furthermore, the internal electric field in the Rashba system can be beneficial to bond anharmonicity and low lattice thermal conductivity. We suggest that bulk materials with large Rashba effect may become potential candidates for efficient thermoelectricity.

DOI: 10.1103/PhysRevB.90.195210 PACS number(s): 72.20.Pa, 71.20.−b, 75.70.Tj

Arising from the atomic spin-orbital coupling (SOC) and inversion asymmetry, the Rashba effect has attracted considerable attention in the fields of spintronics, ferroelectrics, and superconducting electronics [1–6]. To what extent the Rashba-effect-induced spin splitting influences physical properties of solids is a fundamental condensed matter question. SOC gives rise to a perturbing operator equal to $\lambda\vec{L}\cdot\vec{S}$ for electrons, where $\vec{L}$ and $\vec{S}$ are the total orbital and spin angular momenta, and λ the coupling constant [7]. For solids without inversion center, spin can be tuned by internal electric field E_z. The spin-orbital Hamiltonian has a Bychkov-Rashba form $H_{\mathrm{SOC}} = \alpha_R(\vec{\sigma}\times\vec{k})\cdot\vec{z}$, where α_R is the Rashba parameter and represents the strength of the Rashba effect ($\alpha_R \propto \lambda E_z$), $\vec{\sigma}$ the Pauli spin matrices, $\vec{k}$ the momentum, and $\vec{z}$ the electric field direction along the high-symmetry axis [8]. A prototype bulk material with a giant Rashba effect is BiTeI, in which the Rashba spin-splitting bands (RSBs) have been corroborated by the angle-resolved photoemission spectroscopy and first-principles calculations [9,10]. BiTeI becomes a topological insulator with closed band gap under pressure [11–13]. The heat-electricity converting thermoelectric effects are also strongly influenced by the band structures near the Fermi level; thus the Rashba effect may also offer unusual opportunities for thermoelectrics.

The performance of thermoelectric materials is determined by the figure of merit $ZT = S^2T/\rho\kappa$, where S, T, ρ, and κ are the thermopower, absolute temperature, electrical resistivity, and thermal conductivity, respectively [14,15]. Thermopower enhancement without decreasing the carrier concentration (n) is actually a key to excellent thermoelectric materials. The electrical term S^2n has been used to evaluate the intrinsic electrical property of thermoelectric materials [16,17]. Normally the degenerate or converged band structure is favored for large S^2n and good thermoelectric properties [18–20]. SOC can have a significant influence on the thermoelectric properties, like in Bi_2Te_3 [21–23], Mg_2X (X = Si, Ge, Sn) [24], and $LaBiTe_3$ [25]. In materials with inversion symmetry, the bands keep the spin degeneracy regardless of SOC [7]. A Zeeman-like spin splitting with an energy gap of two spins can be induced by SOC in some specific systems [26,27]. In these cases, the thermopower S and S^2n are suppressed as only one spin-polarized band contributes to thermoelectricity. In materials with inversion asymmetry, SOC may result in the Dresselhaus effect [28] and the Rashba effect [29], leading the spin-dependent momentum to shift off the high-symmetry axis. The Rashba effect tends to produce larger spin splitting than the Dresselhaus effect near the band edge, since the former provides a linear shift of the wave vector compared to a third-order change in the latter.

Strikingly, the Rashba spin splitting leads to a unique constant electronic density of states (DOS) due to unique Fermi surface topology [6,30]. The thermopower S and the electrical term S^2n in specific two-dimensional (2D) systems, like 2D quantum wells, were observed to be higher because of the constant DOS [16,31–33]. Thus the Rashba spin splitting can potentially be beneficial to thermoelectric properties. Here we validate the 2D-like thermoelectric properties by experimental and numerical results of bulk BiTeI. The thermopower and electrical term can actually be enhanced in the low-Fermi-energy region because of the constant DOS. A careful theoretical evaluation explicitly shows that larger Rashba splitting strength leads to higher thermopower. Finally, the anharmonicity and low thermal conductivity are addressed in connection with the internal electric field in the Rashba systems.

Polycrystalline BiTeI samples (n-type) were synthesized by a melting-annealing process [34] and densified by spark plasma sintering (SPS). Carrier concentration was adjusted by changing the atomic ratio of Te and I or doping with copper and manganese. Hall measurements were performed on thin bar samples ($2\times9\times0.6\,\mathrm{mm}^3$) in a cryostat equipped with an ac resistance bridge and a 9-T magnet (up to 4 T used in this work). The current (±2 mA) for all Hall measurements was applied perpendicular to the direction of the SPS pressure

*jihuiy@uw.edu

†wqzhang@mail.sic.ac.cn

 ©2014 American Physical Society

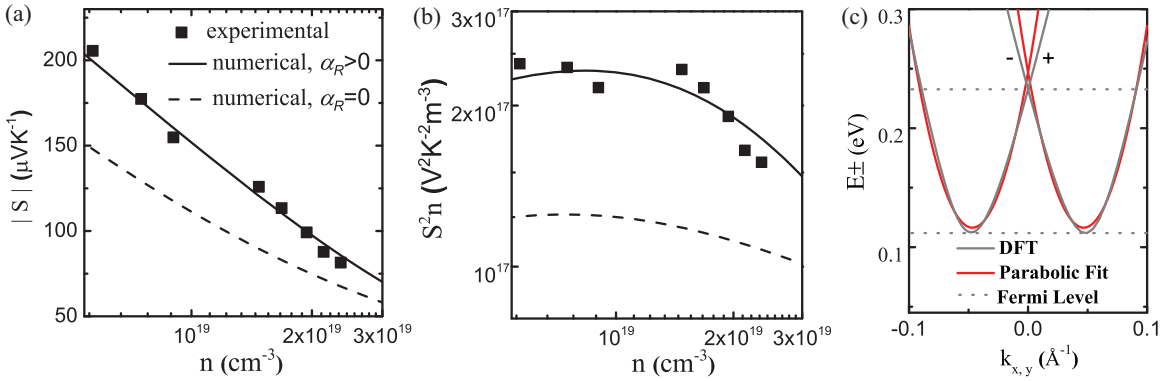

FIG. 1. (Color online) The carrier concentration n-dependent (a) thermopower S and (b) S^2n at 300 K. Filled squares represent the experimental data in bulk BiTeI polycrystals. The solid lines are for the numerical calculations using the Rashba splitting bands (RSBs) with $\alpha_R = 4.3\,\text{eV Å}$. The solid lines also represent calculated results in a 2D quantum well ($L_z = 2.67\,\text{nm}$), while the dashed lines are for the degenerate bands with no Rashba effect ($\alpha_R = 0$). The effective mass is set as $0.19m_e$. (c) The conduction bands of BiTeI. Gray lines are calculated by DFT, while red lines are the parabolic fittings. The dotted lines are the corresponding Fermi levels in the Rashba model for $n = 5.3 \times 10^{18}\,\text{cm}^{-3}$ and $n = 3.4 \times 10^{19}\,\text{cm}^{-3}$ under a parabolic approximation.

while the magnetic field was in parallel. The enhancement of calculated Hall response at low carrier densities, in a previous study, is due to the coexistence of two carriers, i.e., electrons and holes [35]. However, in our Hall measurement of BiTeI, the Hall resistance was always a linear function of the magnetic field with a negative slope, indicating a single charge carrier (electron) dominated electrical transport. The thermopower and resistivity were measured on an ULVAC ZEM-3 system using bar samples ($2.5 \times 2.5 \times 10\,\text{mm}^3$). The thermal conductivity was determined by thermal diffusivity (α), density (D), and heat capacity (C_p) using the equation $\kappa = C_\text{p} \times D \times \alpha$. Thermal diffusivity was measured on a Netzsch LFA-457, vertically to the direction of SPS pressure on square samples with dimensions of $10 \times 10 \times 1.5\,\text{mm}^3$. The Archimedes method was used to measure the density of sintered samples while heat capacity was approximated by the Dulong-Petit law. Calculations of band structures and lattice dynamics were performed using density functional theory (DFT). The modified Becke-Johnson (mBJ) exchange potential [36] and the local density approximation (LDA) [37] were used in the band calculations, where SOC was fully taken into account. The numerical thermopower and carrier concentration were calculated using a parabolic approximation based on a modified Rashba model.

Figure 1 shows the measured room temperature thermopower S and electrical term S^2n as functions of the carrier concentration. The absolute value of thermopower is between 205 and 82 μV/K, when carrier concentration increases from 5.7×10^{18} to $2.4 \times 10^{19}\,\text{cm}^{-3}$. The S^2n is about $2.2 \times 10^{17}\,\text{V}^2\,\text{K}^{-2}\,\text{m}^{-3}$ in the low concentration range and has a weak carrier concentration dependence for $n < 1.5 \times 10^{19}\,\text{cm}^{-3}$ and rapidly decreases when n is higher than $1.5 \times 10^{19}\,\text{cm}^{-3}$. We introduce a theoretical model to interpret the thermoelectric properties of a three-dimensional (3D) Rashba system. We consider the Rashba model [1,6,30] with anisotropic effective mass. The electronic dispersion $E_\pm(k_x,k_y,k_z)$ of a 3D Rashba system is

$$E_\pm(k_x,k_y,k_z) = \frac{\hbar^2}{2m^*_{ab}}\left(\sqrt{k_x^2+k_y^2} \pm k_0\right)^2 + \frac{\hbar^2}{2m^*_c}k_z^2, \quad (1)$$

where k_x, k_y, k_z are the momentum components, k_0 the Rashba momentum, m^*_{ab} (m^*_c) the effective mass of electrons in the ab plane (along the c axis), and $\hbar$ the reduced Planck constant. The Rashba parameter α_R can be expressed as $\alpha_R = \hbar^2 k_0/m^*_{ab}$. The electronic dispersion will become spin degenerated with the Rashba parameter $\alpha_R = 0$, which is the case in normal bulk systems. For the 3D Rashba systems ($\alpha_R > 0$), the Fermi surface has an elliptic-torus shape when the Fermi energy E_F is smaller than the Rashba energy $E_0 = \hbar^2 k_0^2/2m^*_{ab}$ (energy of the band-crossing point, i.e., the Dirac point). The volume of the Rashba spin-splitting carrier pocket has the form $V = 2^{5/2}\pi^2 (m^*)^{3/2} E_0^{1/2} E_F/\hbar^3$, where $m^* = [(m^*_{ab})^2 m^*_c]^{1/3}$ is the effective mass (Appendix). The corresponding DOS therefore becomes a constant as $N(E) = [dV/dE_F]/(2\pi)^3$ [38], which can be expressed as

$$N(E) = \frac{(m^*)^{3/2} E_0^{1/2}}{2^{1/2}\pi\hbar^3}. \quad (2)$$

The DOS has the same expression in systems with no anisotropy ($m^*_{ab} = m^*_c$) [6]. A quantum well with the thickness $L_z = 2^{1/2}\hbar/(m^* E_0)^{1/2}$ has the same DOS value as Eq. (2), since the DOS in a quantum well is expressed as $N^\text{QW}(E) = m^*/\pi\hbar^2 L_z$ [39]. With the Fermi level higher than E_0 in the 3D Rashba system, DOS increases with increasing energy [6], close to those of normal bulk materials.

Taking the relaxation time $\tau(E) = \tau_0 E^r$, where τ_0 is a constant and r the scattering parameter, we can obtain expressions for thermopower S and carrier concentration n in a 3D Rashba system ($E_F < E_0$) using the transport theory [40,41]. The thermopower S and carrier concentration n can be expressed as

$$S = \pm\frac{k}{e}\left[\eta - \frac{(r+2)F_{r+1}(\eta)}{(r+1)F_r(\eta)}\right], \quad (3)$$

$$n = \frac{kT(m^*)^{3/2}E_0^{1/2}}{2^{1/2}\pi\hbar^3}F_0(\eta), \quad (4)$$

where $\eta = E_F/kT$ is the reduced Fermi energy, k the Boltzmann constant, and $F_n(\eta)$ the nth Fermi-Dirac integral $F_n(\eta) = \int_0^\infty \xi^n/[\exp(\xi-\eta)+1]d\xi$.

BiTeI has been proved to be a 3D material with a giant Rashba effect. The Fermi surface of BiTeI varies topologically with the Fermi level, from a spindle torus ($E_F > E_0$) to a ring or elliptic torus ($E_F < E_0$) [42]. First-principles calculations clearly revealed the band structure of BiTeI, showing the momentum offset $k_0 = 0.05\,\text{Å}^{-1}$ and Rashba energy $E_0 = 0.113\,\text{eV}$, comparable to the experimental results [9,10]. The corresponding Rashba parameter α_R is 4.3 eV Å. Our DFT calculations reveal similar band structures and Rashba parameters, as shown in Fig. 1(c). The conduction bands of BiTeI are close to a parabolic shape below the Dirac point. The Rashba model can thus be used in the BiTeI system by taking the parabolic approximation. The thermopower and carrier concentration of BiTeI were calculated using Eqs. (3) and (4). The effective mass m^* of BiTeI near the Dirac point is around $0.19m_e$ with m_e being the free electron mass [43]. The scattering parameter r is essential for thermopower analysis, which equals -0.5 and 1.5 for acoustic phonon and ionized impurity scattering, respectively. Some BiTeI single crystals showed a carrier scattering process by acoustic phonons [44,45]. However, the mobility of our polycrystals shows a weak temperature dependence like the previous report [46], due to a combination of these two scattering processes near room temperature. We have set $r = 0$ for numerical calculations of the carrier concentration–dependent thermopower S and S^2n at 300 K, shown as the solid lines in Fig. 1. The numerical results turn out to be quite close to the experimental data with $r = 0$. This intermediate value of scattering parameter [47] is consistent with the temperature dependence of mobility. When the carrier concentration increases from 5.3×10^{18} to $3.0 \times 10^{19}\,\text{cm}^{-3}$, the absolute value of thermopower decreases from 205 to 69.2 μV/K. Using the band structure parameters, we find that the bulk BiTeI has the same DOS as in a 2.67-nm-thick quantum well with the same effective mass $m^* = 0.19m_e$. The calculated thermopower S and electrical term S^2n of this quantum well follow exactly the solid lines in Fig. 1, substantiating the 2D thermopower nature in 3D Rashba BiTeI.

To reveal the contribution of the unique spin-splitting bands, the dashed lines in Fig. 1 are plotted for the normal spin-degenerated case ($\alpha_R = 0$) found in many traditional thermoelectric materials, like Bi_2Te_3. The thermoelectric theory for a degenerate single parabolic band has been well established and verified in many thermoelectric materials [48]. In the case of $\alpha_R = 0$, we fix the effective mass and the band shape is exactly the same as the Rashba bands. The only difference is the zero momentum shift for both spin states. The thermopower S and S^2n in the 3D Rashba system ($\alpha_R > 0$) are larger than those in the normal bulk materials ($\alpha_R = 0$) at any given carrier concentration. Figure 1(b) shows that the maximum value of S^2n is $2.3 \times 10^{17}\,\text{V}^2\,\text{K}^{-2}\,\text{m}^{-3}$ in the Rashba system, nearly twice those in normal materials.

The 3D features are no longer held for the Rashba systems. The mechanism for the constant DOS is totally different with that of quantum wells. The DOS in quantum wells is related to the quantum confinement in one direction, while the 2D-like DOS in a 3D Rashba system comes from the strong SOC and electric field along the polar axis. The Fermi energy–dependent DOS and n in the 3D Rashba material BiTeI have been numerically calculated, as shown in Figs. 2(a) and 2(b). The DOS of BiTeI has been measured by angle-integrated photoemission spectroscopy (PES) [9]. When the binding energy is between the band minimum and the Dirac point, the intensity of angle-integrated PES is essentially a constant. The experimental results in Fig. 2(a) agree with the calculated DOS function in the Rashba model ($\alpha_R > 0$), yet totally different from that determined with $\alpha_R = 0$. Carrier concentration is another probe for the 2D-like DOS. As shown in Fig. 2(b), the DFT calculations [35] illustrate that BiTeI has high carrier concentration ($10^{18} - 10^{19}\,\text{cm}^{-3}$) at a given Fermi energy in the low-energy region. Numerical results indicate that the 3D Rashba model gives comparable carrier concentrations with the DFT calculations, while the single parabolic band model ($\alpha_R = 0$) significantly underestimates the carrier concentration, even with an effective mass of $0.28m_e$. The high thermopower in the Rashba systems is a direct result of their 2D-like DOS. In degenerate bands, the Fermi surface is generally an ellipsoid, whose volume can be expressed as $V_0(E) = 2^{7/2}\pi(m^*)^{3/2}E^{3/2}/3\hbar^3$. Considering the spin degeneracy, the ratio of carrier concentration in Rashba materials (n) and the degenerate systems (n_0) becomes $n/n_0 = V(E_F)/2V_0(E_F) = 3\pi/4(E_0/E_F)^{1/2}$. In the low-Fermi-energy region $E_F < E_0$, the spin-splitting carrier pocket in the Rashba bands is more than twice as large as the

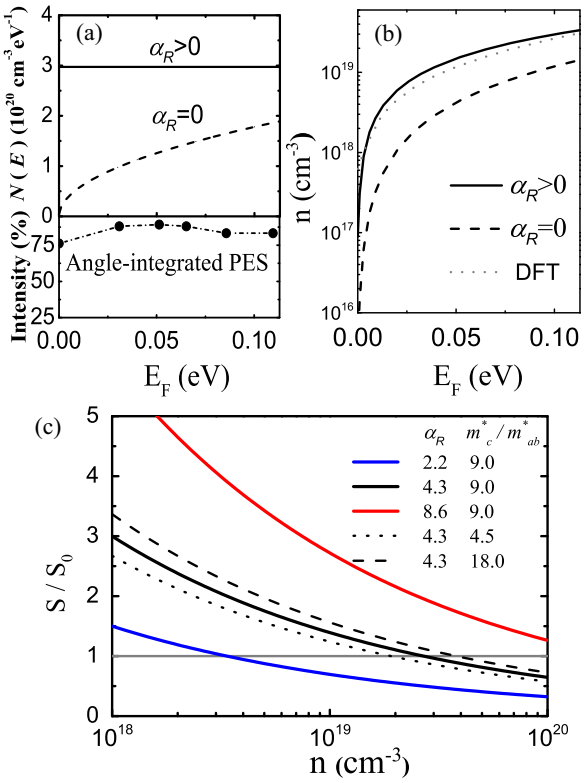

FIG. 2. (Color online) (a) Calculated density of states ($\alpha_R > 0$ and $\alpha_R = 0$), compared with results of angle-integrated photoemission spectroscopy (PES) in BiTeI at 6 K [9]. (b) Carrier concentrations numerically calculated for $\alpha_R > 0$ and $\alpha_R = 0$ at 5 K, compared with DFT calculation results [35]. (c) The ratio of thermopower $S(\alpha_R > 0)$ and $S_0(\alpha_R = 0)$ with different Rashba parameters (α_R in eV Å) and effective mass anisotropies (m_c^*/m_{ab}^*). Degenerate approximation is used and the horizontal line represents $S/S_0 = 1$.

degenerate one. Assuming the same carrier concentration, the Fermi level is much lower for materials with the Rashba effect. Figure 2(b) illustrates the Fermi energy differences for $\alpha_R > 0$ and $\alpha_R = 0$ in the carrier concentration range. The lower Fermi level leads to higher thermopower in the 3D Rashba systems, just like in quantum wells.

Direct connection between the 2D-like thermopower and the Rashba splitting strength could be established quantitatively by taking the degenerate approximation ($\eta \gg 1$). With $r = 0$, the carrier concentration–dependent thermopower in RSB can be expressed as

$$S = \pm \frac{\pi k^2 T}{3\sqrt{2} e\hbar^3} \frac{(m^*)^{3/2} E_0^{1/2}}{n}. \quad (5)$$

Equation (5) shows that materials with large Rashba energy E_0 will have higher thermopower, given the same carrier concentration and effective mass. The thermopower in spin-degenerated bands has the form

$$S_0 = \pm \frac{5\pi^2 k^2 T}{4(3\pi^2)^{2/3} e\hbar^2} \frac{m^*}{n^{2/3}}. \quad (6)$$

Thermopower is apparently more sensitive to carrier concentration in the Rashba system, as S is proportional to n^{-1} instead of $n^{-2/3}$ (common in thermoelectric materials). The ratio of the two thermopowers can be expressed as

$$\frac{S}{S_0} = \frac{2(3\pi^2)^{2/3} m^*_{ab}}{15\pi\hbar^2} \frac{(m^*_c/m^*_{ab})^{1/6} \alpha_R}{n^{1/3}}. \quad (7)$$

The condition for the degenerate approximation is that the Fermi energy is much larger than kT. Equation (7) explicitly relates thermopower with the Rashba parameter α_R. Figure 2(c) shows the carrier concentration–dependent S/S_0 ratio with different α_R and anisotropy of effective mass m^*_c/m^*_{ab}, where the Fermi level is assumed to locate below the Dirac point and an in-plane effective mass $m^*_{ab} = 0.09m_e$ [49] is used. It is clear that large Rashba parameter and high anisotropy are preferred for achieving large 2D-like thermopower. Compared with the anisotropy, α_R is the dominant factor influencing thermopower of the Rashba systems. Since DOS is larger with stronger Rashba splitting (larger α_R), the Fermi energy is then substantially lower for the same carrier concentration, resulting in larger thermopower. Herein we focused on the 2D-like electrical properties with Fermi level below the Dirac point. The thermoelectric transports of BiTeI have been measured at higher carrier concentrations, which correspond to the 3D-like DOS (Fermi level above the Dirac point) [45].

Rashba systems all have dipole electrical fields, at least on the atomic sites [50]. The dipole fields also affect their lattice vibrational behavior by introducing anharmonicity and soft bonds, analog to the case of near-ferroelectric material PbTe [51]. In BiTeI, our DFT analysis [52] shows charge density accumulation between the Bi and Te atoms indicative of strong covalent bonds; the bonds of I atoms, however, are more ionic. The internal electrical field E_z in BiTeI is aligned along the c direction, from the positive $(BiTe)^+$ layers to negative I^- layers as shown in Fig. 3(a), consistent with the previous discussion [34]. The electrical field is fundamentally caused by the asymmetric chemical environment, which in turn affects

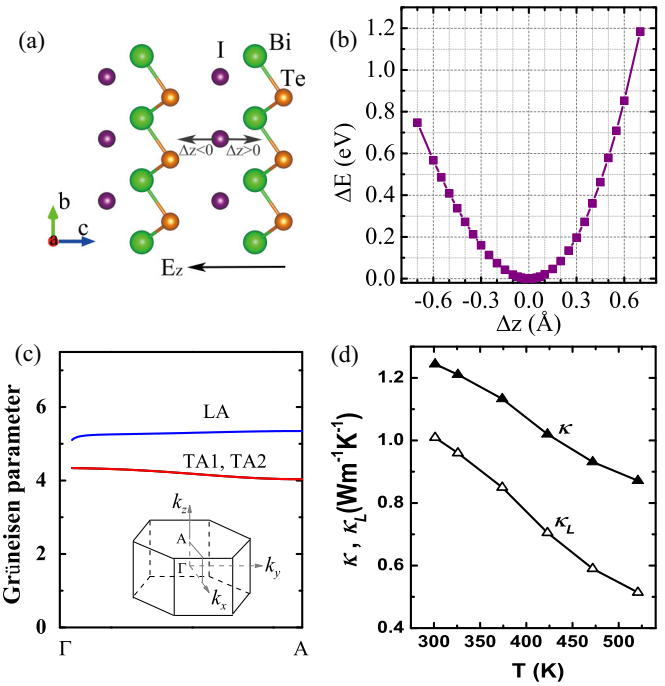

FIG. 3. (Color online) (a) Crystal structure of BiTeI. The internal electrical field E_z and I atomic displacement Δz are along the c direction. (b) Potential well ΔE as a function of the I atomic displacements. (c) Mode Grüneisen parameter along the ΓA direction (the same direction as E_z) for longitudinal acoustic (LA) mode and transverse acoustic (TA1 and TA2) modes. (d) Measured thermal conductivity κ and lattice thermal conductivity κ_L of undoped BiTeI polycrystal.

the local atomic motions, especially for the ionic I atoms. Figure 3(b) shows the potential well ΔE of one I atom in a supercell, with respect to its displacement Δz along the c direction. The ΔE difference at both sides of its equilibrium is 0.4 eV at the displacements of ± 0.7 Å, indicating a dipole field of $\sim 2.9 \times 10^4$ kV/cm, comparable to those in $\alpha-$SnTe [50]. The anharmonic local atomic motions give rise to anharmonic acoustic phonon modes, which can be directly shown by the mode Grüneisen parameters [Fig. 3(c)], obtained by using the DFT phonon methodology [53]. The values are as large as ~ 4.0 for the two degenerate transverse acoustic (TA1 and TA2) modes and ~ 5.5 for the longitudinal acoustic (LA) mode along the k_z direction. Lattice thermal conductivity κ_L of the undoped BiTeI sample is calculated from measured thermal conductivity by the Wiedemann-Franz law [7] with the Lorenz number of 2.4×10^{-8} V^2 K^{-2}, which is as low as 1 W m^{-1} K^{-1} at 300 K and 0.5 W m^{-1} K^{-1} at 520 K, shown in Fig. 3(d). The low thermal conductivity is closely related to the large Grüneisen parameters (strong anharmonicity) induced by the internal electrical field and low group velocities brought by soft bonds among the constituent elements.

Figure 4 shows the temperature-dependent thermopower S and resistivity ρ of undoped BiTeI sample between 300 and 520 K. As shown in Fig. 4(a), we could fit the S-T curve well with a scattering parameter $r = -0.13$. The scattering parameter r is close to 0, which is consistent with the S–n relation and further corroborates the mixed scattering of electrons in BiTeI. The figure of merit ZT at 300 K, shown

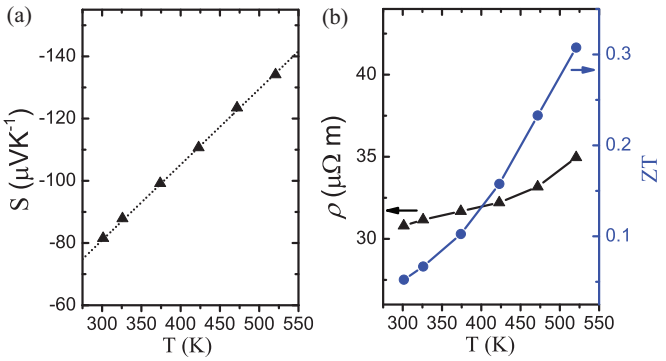

FIG. 4. (Color online) The measured thermopower S, resistivity ρ, and figure of merit ZT of undoped BiTeI in the temperature range of 300–520 K. The dotted line in (a) shows the fitting with $r = -0.13$.

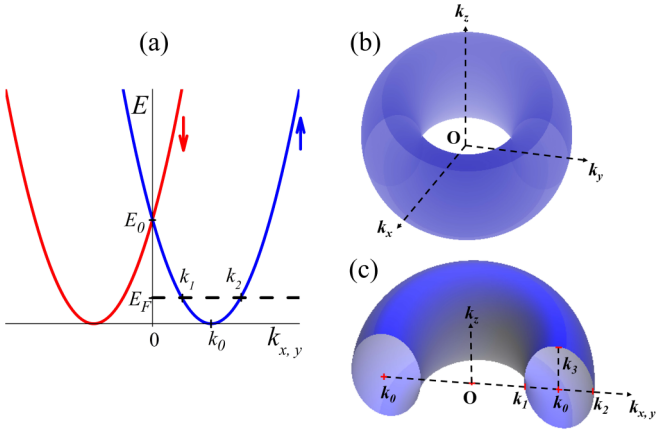

FIG. 5. (Color online) (a) Band structure of the Rashba system in the $k_z = 0$ plane. The arrows show the different spin states. (b) The Fermi surface with an elliptic-torus shape ($E_F < E_0$). (c) The ellipse-shaped cross section of the carrier pocket.

in Fig. 4(b), is 0.05, lower than the sister compound BiTeCl grown by the topotactic method [54]. The ZT of undoped BiTeI reaches 0.3 at 520 K, primarily limited by its low mobility ($\sim$86 cm^2 V^{-1} s^{-1} at 300 K). Because the specific heat was approximated by the Dulong-Petit law, thermal conductivity and ZT values presented may be underestimated and overestimated by about 10%–20% at high temperatures, respectively. By reducing impurity scatterings [55], the overall thermoelectric properties may still be improved.

Recent work shows that hidden Rashba effect may exist in centrosymmetric crystals with local dipole field, which broadens the range of Rashba materials [50]. To date, bulk materials with strong Rashba effect all have narrow band gaps [5,50,56], which is ideal for electrical properties in thermoelectrics [57]. Heavy atomic mass in Rashba materials also contributes to the low lattice thermal conductivity. We suggest that bulk Rashba materials may possess good overall thermoelectric performance. We further speculate that high thermoelectric performance of p-type GeTe-based materials [58] with the noncentrosymmetric $R3m$ space group may partially be related to the Rashba effect [5], as the valence band top has large spin splitting.

In conclusion, we have studied 2D-like thermoelectric properties of a 3D bulk Rashba system. A general model is introduced for calculating thermopower of bulk materials with the Rashba spin-splitting bands. The 2D thermopower in the Rashba systems is larger than that in normal materials at given carrier concentrations, which is attested in bulk BiTeI. The unique topology of the Fermi surface provides large carrier pockets and the thermopower is higher because of the lower Fermi level. We find that larger Rashba strength leads to higher thermopower and thermoelectric performance. The anharmonic vibrational behavior and low thermal conductivity in BiTeI has also been discussed in connection with the internal electrical field. Our results call for the search of new bulk thermoelectric materials with strong Rashba effect.

L.W. would like to thank Dr. Yi Zhang for fruitful discussions, and China Scholarship Council for support. This work was supported by US Department of Energy under Corporate Agreement No. DE-FC26-04NT42278, by GM, and by National Science Foundation under Award No. 1235535. W.Z. acknowledges support by National Basic Research Program (973-program) of China under Project No. 2013CB632501, and by Natural Science Foundation of China under Grant No. 11234012.

APPENDIX: CARRIER POCKET VOLUME OF RASHBA BANDS

The band minimum of Rashba bands shifts off the high-symmetry point, as shown in Fig. 5(a). When the Fermi level is below the Dirac point ($E_F < E_0$), the Fermi surface is a toroid or a ring torus [6,30]. Herein we consider the anisotropy of effective mass, as shown in Eq. (1). The Fermi surface is an elliptic torus, as shown in Fig. 5(b). In order to calculate the pocket volume, the ellipse-shaped cross section of the carrier pocket is shown in Fig. 5(c). We can obtain the area A of the ellipse-shaped cross section using

$$A = \pi k_3 (k_2 - k_1)/2, \tag{A1}$$

where k_3 is the minor semiaxis for the ellipse in the k_z direction and $[(k_2 - k_1)/2]$ is the major semiaxis along the $k_{x,y}$ direction. The volume contained by the elliptic torus [59] is

$$V = 2\pi k_0 A. \tag{A2}$$

Given the Fermi energy E_F in Eq. (1), we can get the corresponding momentum k_1 and k_2 in the $k_z = 0$ plane as follows:

$$k_1 = k_0 - \left(\frac{2m^*_{ab} E_F}{\hbar^2}\right)^{1/2}, \tag{A3}$$

$$k_2 = k_0 + \left(\frac{2m^*_{ab} E_F}{\hbar^2}\right)^{1/2}, \tag{A4}$$

which are shown in Fig. 5(a). From Eq. (1) with the given Fermi energy E_F, $k_{x,y}$ should be equal to k_0 in order to obtain the maximum momentum k_3 along the k_z direction [shown in Fig. 5(c)]. We can get the expression for the momentum k_3 as

$$k_3 = \left(\frac{2m^*_c E_F}{\hbar^2}\right)^{1/2}. \tag{A5}$$

Taking Eqs. (A3)–(A5) into Eq. (A1), we get the area of the cross section as

$$A = \frac{2\pi (m^*_{ab} m^*_c)^{1/2}}{\hbar^2} E_F. \quad \text{(A6)}$$

Using Eqs. (A2) and (A6), the volume of the carrier pocket can be expressed as

$$V = \frac{2^{5/2}\pi^2 (m^*)^{3/2} E_0^{1/2}}{\hbar^3} E_F, \quad \text{(A7)}$$

where $m^* = [(m^*_{ab})^2 m^*_c]^{1/3}$ is the effective mass.

[1] E. I. Rashba, Sov. Phys. Solid State **2**, 1109 (1960).
[2] S. Datta and B. Das, Appl. Phys. Lett. **56**, 665 (1990).
[3] S. Mathias, A. Ruffing, F. Deicke, M. Wiesenmayer, I. Sakar, G. Bihlmayer, E. V. Chulkov, Y. M. Koroteev, P. M. Echenique, M. Bauer, and M. Aeschlimann, Phys. Rev. Lett. **104**, 066802 (2010).
[4] J. Park, S. W. Jung, M.-C. Jung, H. Yamane, N. Kosugi, and H. W. Yeom, Phys. Rev. Lett. **110**, 036801 (2013).
[5] D. Di Sante, P. Barone, R. Bertacco, and S. Picozzi, Adv. Mater. **25**, 509 (2013).
[6] E. Cappelluti, C. Grimaldi, and F. Marsiglio, Phys. Rev. Lett. **98**, 167002 (2007).
[7] J. M. Ziman, *Principles of the Theory of Solids* (Cambridge University Press, London, 1972).
[8] Y. A. Bychkov and E. I. Rashba, JETP Lett. **39**, 78 (1984).
[9] K. Ishizaka, M. S. Bahramy, H. Murakawa, M. Sakano, T. Shimojima, K. K. T. Sonobe, S. Shin, H. Miyahara, A. Kimura, K. Miyamoto, T. Okuda, H. Namatame, M. Taniguchi, R. Arita, N. Nagaosa, K. Kobayashi, Y. Murakami, R. Kumai, Y. Kaneko, Y. Onose *et al.*, Nat. Mater. **10**, 521 (2011).
[10] M. S. Bahramy, R. Arita, and N. Nagaosa, Phys. Rev. B **84**, 041202 (2011).
[11] M. K. Tran, J. Levallois, P. Lerch, J. Teyssier, A. B. Kuzmenko, G. Autès, O. V. Yazyev, A. Ubaldini, E. Giannini, D. van der Marel, and A. Akrap, Phys. Rev. Lett. **112**, 047402 (2014).
[12] M. Bahramy, B.-J. Yang, R. Arita, and N. Nagaosa, Nat. Commun. **3**, 679 (2012).
[13] X. Xi, C. Ma, Z. Liu, Z. Chen, W. Ku, H. Berger, C. Martin, D. B. Tanner, and G. L. Carr, Phys. Rev. Lett. **111**, 155701 (2013).
[14] G. J. Snyder and E. S. Toberer, Nat. Mater. **7**, 105 (2008).
[15] J. Yang, H.-L. Yip, and A. K.-Y. Jen, Adv. Energy Mater. **3**, 549 (2013).
[16] M. S. Dresselhaus, G. Chen, M. Y. Tang, R. G. Yang, H. Lee, D. Z. Wang, Z. F. Ren, J. P. Fleurial, and P. Gogna, Adv. Mater. **19**, 1043 (2007).
[17] J. P. Heremans, B. Wiendlocha, and A. M. Chamoire, Energy Environ. Sci. **5**, 5510 (2012).
[18] Y. Pei, X. Shi, A. LaLonde, H. Wang, L. Chen, and G. J. Snyder, Nature **473**, 66 (2011).
[19] J. Zhang, R. Liu, N. Cheng, Y. Zhang, J. Yang, C. Uher, X. Shi, L. Chen, and W. Zhang, Adv. Mater. **26**, 3848 (2014).
[20] W. Liu, X. Tan, K. Yin, H. Liu, X. Tang, J. Shi, Q. Zhang, and C. Uher, Phys. Rev. Lett. **108**, 166601 (2012).
[21] P. Larson, S. D. Mahanti, and M. G. Kanatzidis, Phys. Rev. B **61**, 8162 (2000).
[22] T. J. Scheidemantel, C. Ambrosch-Draxl, T. Thonhauser, J. V. Badding, and J. O. Sofo, Phys. Rev. B **68**, 125210 (2003).
[23] S. J. Youn and A. J. Freeman, Phys. Rev. B **63**, 085112 (2001).
[24] K. Kutorasinski, B. Wiendlocha, J. Tobola, and S. Kaprzyk, Phys. Rev. B **89**, 115205 (2014).
[25] N. Singh and U. Schwingenschlögl, Phys. Status Solidi RRL **08**, 805 (2014).
[26] Y. Zhang, X. Ke, C. Chen, J. Yang, and P. R. C. Kent, Phys. Rev. Lett. **106**, 206601 (2011).
[27] H. J. Xiang and D. J. Singh, Phys. Rev. B **76**, 195111 (2007).
[28] G. Dresselhaus, Phys. Rev. **100**, 580 (1955).
[29] E. I. Rashba, Sov. Phys. Solid State **1**, 368 (1959).
[30] R. Casella, Phys. Rev. Lett. **5**, 371 (1960).
[31] L. D. Hicks and M. S. Dresselhaus, Phys. Rev. B **47**, 12727 (1993).
[32] D. J. Singh, Phys. Rev. B **61**, 13397 (2000).
[33] D. Parker, X. Chen, and D. J. Singh, Phys. Rev. Lett. **110**, 146601 (2013).
[34] A. V. Shevelkov, E. V. Dikarev, R. V. Shpanchenko, and B. A. Popovkin, J. Solid. State. Chem. **114**, 379 (1995).
[35] L. Demkó, G. A. H. Schober, V. Kocsis, M. S. Bahramy, H. Murakawa, J. S. Lee, I. Kézsmárki, R. Arita, N. Nagaosa, and Y. Tokura, Phys. Rev. Lett. **109**, 167401 (2012).
[36] F. Tran and P. Blaha, Phys. Rev. Lett. **102**, 226401 (2009).
[37] J. P. Perdew and Y. Wang, Phys. Rev. B **45**, 13244 (1992).
[38] N. D. M. Neil and W. Ashcroft, *Solid State Physics* (Harcourt College Publishers, Orlando, FL, 1976).
[39] D. A. Miller, *Quantum Mechanics for Scientists and Engineers* (Cambridge University Press, New York, 2008).
[40] H. J. Goldsmid, *Introduction to Thermoelectricity* (Springer-Verlag, Berlin Heidelberg, 2009).
[41] A. Shakouri, Annu. Rev. Mater. Res. **41**, 399 (2011).
[42] G. Landolt, S. V. Eremeev, Y. M. Koroteev, B. Slomski, S. Muff, T. Neupert, M. Kobayashi, V. N. Strocov, T. Schmitt, Z. S. Aliev, M. B. Babanly, I. R. Amiraslanov, E. V. Chulkov, J. Osterwalder, and J. H. Dil, Phys. Rev. Lett. **109**, 116403 (2012).
[43] C. Martin, E. D. Mun, H. Berger, V. S. Zapf, and D. B. Tanner, Phys. Rev. B **87**, 041104 (2013).
[44] A. Tomokiyo, T. Okada, and S. Kawano, Jpn. J. Appl. Phys. **16**, 291 (1977).
[45] V. A. Kulbachinskii, V. G. Kytin, A. A. Kudryashov, A. N. Kuznetsov, and A. V. Shevelkov, J. Solid State. Chem. **193**, 154 (2012).
[46] N. T. Dich, P. Lostak, and J. Horak, Czech. J. Phys. B **28**, 1297 (1978).
[47] G. A. Slack and M. A. Hussain, J. Appl. Phys. **70**, 2694 (1991).
[48] A. Ioffe, *Semiconductor Thermoelements and Thermoelectric Cooling* (Infosearch Limited, London, 1957).
[49] S. Bordács, J. G. Checkelsky, H. Murakawa, H. Y. Hwang, and Y. Tokura, Phys. Rev. Lett. **111**, 166403 (2013).
[50] X. Zhang, Q. Liu, J.-W. Luo, A. Freeman, and A. Zunger, Nat. Phys. **10**, 387 (2014).
[51] Y. Zhang, X. Ke, P. R. C. Kent, J. Yang, and C. Chen, Phys. Rev. Lett. **107**, 175503 (2011).

[52] L. Xi, Y. B. Zhang, X. Y. Shi, J. Yang, X. Shi, L. D. Chen, W. Zhang, J. Yang, and D. J. Singh, Phys. Rev. B **86**, 155201 (2012).

[53] Y. Zhang, E. Skoug, J. Cain, V. Ozoliņš, D. Morelli, and C. Wolverton, Phys. Rev. B **85**, 054306 (2012).

[54] J. Jacimovic, X. Mettan, A. Pisoni, R. Gaal, S. Katrych, L. Demko, A. Akrap, L. Forro, H. Berger, and P. Bugnon, Scr. Mater. **76**, 69 (2014).

[55] C.-R. Wang, J.-C. Tung, R. Sankar, C.-T. Hsieh, Y.-Y. Chien, G.-Y. Guo, F. Chou, and W.-L. Lee, Phys. Rev. B **88**, 081104(R) (2013).

[56] M. Sakano, M. S. Bahramy, A. Katayama, T. Shimojima, H. Murakawa, Y. Kaneko, W. Malaeb, S. Shin, K. Ono, H. Kumigashira, R. Arita, N. Nagaosa, H. Y. Hwang, Y. Tokura, and K. Ishizaka, Phys. Rev. Lett. **110**, 107204 (2013).

[57] J. O. Sofo and G. D. Mahan, Phys. Rev. B **49**, 4565 (1994).

[58] C. Wood, Rep. Prog. Phys. **51**, 459 (1988).

[59] A. Gray, E. Abbena, and S. Salamon, *Modern Differential Geometry of Curves and Surfaces with Mathematica* (CRC Press, Boca Raton, FL, 1997).